Synchrotron-based x ray fluorescence ghost imaging

Mathieu Manni,[1,2] Adi Ben-Yehuda,[2] Yishai Klein,[2] [ID] Bratislav Lukic,[1] Andrew Kingston,[3] [ID] Alexander Rack,[1] [ID] Sharon Shwartz,[2] and Nicola Viganò[1,4,*] [ID]

[1] ESRF — The European Synchrotron, Grenoble 38043, France
[2] Physics Department and Institute of Nanotechnology and Advanced Materials, Bar Ilan University, Ramat Gan 52900, Israel
[3] Department of Materials Physics, Research School of Physics, The Australian National University, Canberra, ACT 2601, Australia
[4] IRIG-MEM, CEA, Université Grenoble Alpes, Grenoble 38000, France
*nicola.vigano@cea.fr

X ray fluorescence ghost imaging (XRF-GI) was recently demonstrated for x ray lab sources. It has the potential to reduce the acquisition time and deposited dose by choosing their trade-off with a spatial resolution while alleviating the focusing constraints of the probing beam. Here, we demonstrate the realization of synchrotron-based XRF-GI: we present both an adapted experimental setup and its corresponding required computational technique to process the data. This extends the above-mentioned potential advantages of GI to synchrotron XRF imaging. In addition, it enables new strategies to improve resilience against drifts at all scales and the study of previously inaccessible samples, such as liquids.   © 2023 Optica Publishing Group

---

Introduction. X ray fluorescence (XRF) is used in a wide variety of experimental techniques, including two- and three-dimensional chemical mappings spanning a large range of scales. It is used for sample characterization in a multitude of application areas, including material science [1], chemistry [2], and cultural heritage [3]. The chemical sensitivity of XRF is achieved through the excitation of core electrons: when the excited atoms return to lower excitation states, they emit secondary photons with characteristic energies, which uniquely depend on the atomic number. Energy-resolving detectors (routinely used in x ray measurements) can discriminate these photons with sufficient energy resolution, to identify the element from which they originated. XRF imaging is usually achieved by scanning the samples with a focused beam (pencil beam, PB) and by collecting the emitted XRF signal (spectrum) with single-pixel energy-resolving detectors. The collected XRF spectra are then processed to fit the measured local chemical composition [4].

PB acquisitions require raster scanning (sequentially) of all points in the field of view (FoV) by transversely displacing the sample. Each exposure has an associated XRF spectrum, which corresponds to one pixel in the resulting spectral image. Synchrotron radiation, compared to x ray tube-based sources, is characterized by higher photon flux and (on long beamlines) spatial coherence. This enables reaching x ray beam waists of tens of nm with a high photon flux [5], which, in turn, enables the study of micro- and nano-structured samples with unrivaled

speeds, compared to laboratory sources. As it delivers a high radiation dose rate per unit surface per unit time, it can cause serious localized damage and deformation in sensitive samples. Heat can also contribute to positional drifts and uncertainties, potentially leading to image degradation.

In contrast to PB, classical ghost imaging (GI) acquisitions illuminate the entire FoV. Differently from other full-field techniques [6,7], it does so with different structured beams at each exposure [8]. For x rays, these structured beams are usually obtained by inserting non-configurable transversely displaced structuring masks in the beam, to encode the spatial information in the acquired GI signals. In the specific case of XRF-GI, the XRF detector records the spectrum associated with each illumination pattern. The XRF energy emission lines corresponding to different chemical elements are reconstructed into spatially resolved maps, using computational imaging algorithms. GI acquires spatial information on the whole FoV at each realization. Thanks to the inherent compressibility of natural images, it is possible to acquire fewer realizations than the number of pixels in the reconstructed image, leading to reduced dose deposition, which is not possible with PB scans [9]. The sole translation of the masks in XRF-GI, compared to the translation of the samples for PB, enables the study of previously inaccessible samples like liquids that cannot move during measurements. Moreover, by spreading the beam flux over the entire FoV (as opposed to just the focal spot in PB), XRF-GI could offer more efficient mitigation of dose effects (e.g., easier cooling) and reduce the localized radiation-induced damage. Despite having first developed XRF-GI on laboratory equipment [10], the transposition to synchrotron beamlines is highly desirable, even though it comes with its own challenges.

X ray GI image reconstructions require the mask shapes and positions, and the incident beam intensity to be known. In contrast to x ray tubes (used in laboratory x ray setups) that are characterized by rather stable emission fluxes over time, synchrotron sources exhibit beam-intensity decay. Even in the top-up mode, flux variations of up to 10% can be observed. Beam monitors are usually placed upstream of the masks. However, the masks create unknown and variable attenuation between the diode and the sample, which render calibration of the XRF signal difficult or impossible. The mask shapes can be known by measuring them before the scans or knowing their design from fabrication (computational GI); splitting the structured beam
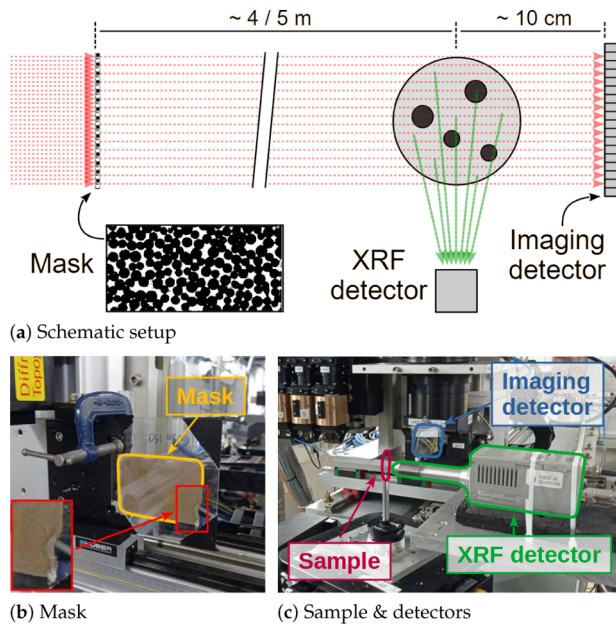
Fig. 1. (a) Schematic synchrotron XRF-GI setup; (b) CuSn mask, whose corner is shown in the inset on the bottom left; and (c) sample, imaging detector with Si attenuation wafers, and XRF detector.

with a beamsplitter positioned after the masks; and measuring the beam that does not impinge on the sample (Classical GI) [11–13]. On synchrotron beamlines, cameras with sub-µm or few µm pixel sizes are routinely used. With slight instability of the beam direction and sample drifts, misalignment artifacts are more likely to manifest, which negatively impacts both the above-mentioned approaches.

Here, we demonstrate a synchrotron-based XRF-GI implementation that does not require knowing or measuring the masks in advance, to split the structured beam, calibrating with high-precision of positions of the masks, nor using a beam monitor to track possible incident beam-intensity variations.

Experimental setup. The experimental setup is presented in Fig. 1. A large structuring mask is positioned on a translation stage in the x ray beam upstream of the sample. At each GI realization, the synchrotron x ray beam only illuminates a portion of the mask, producing the corresponding illuminating beam shape. Different beam shapes are obtained by translating the mask transversely with respect to the incoming beam. A 2D imaging detector is positioned downstream of the sample, and an XRF single-pixel detector is positioned next to the sample, perpendicular to the incoming beam direction. We demonstrate our setup on the ID19 beamline of the ESRF — the European Synchrotron, using a $1 \times 2\,mm^2$ incident beam size. The imaging detector is a so-called Hasselblad system, with two identical lenses (100 mm focal length) in tandem configuration (giving $\sim \times 1$ magnification), with a 500 µm LuAG:Ce scintillator and a "pco.edge 5.5" camera. It is positioned $\sim$ 10 cm downstream of the sample, with an effective pixel size of 6 µm. A large mask, composed of a monolayer of randomly distributed CuSn (bronze) spheres (average diameter $\sim$ 50 µm and maximum diameter $\sim$ 150 µm), is positioned $\sim 4 - 5$ m upstream of the sample. The incoming beam energy is $\sim$ 26 keV, given by the beamline's single-harmonic undulator (type: u13), without the use of a monochromator. The XRF detector is a "Hitachi Vortex 90EX" single-pixel detector, controlled by a "XIA FalconX"

module. The sample is composed of two Cu flattened wires and one Fe 50 µm thick wire, stored in a capillary. The capillary is mostly made of plastic, with heavier trace elements.

Acquisition procedure. In [10], the imaging and XRF detectors acquired their respective signals separately. The sample needed to be removed from the FoV to acquire the beam structures. Thus, the same scan was performed two times: one with the sample in the FoV, using the XRF detector, and one without the sample in the FoV, using the imaging detector. This exposed one of the two measurements to positioning and flux estimation errors with respect to the other.

In this new implementation, the two detectors simultaneously acquire their respective signals (for the same time duration). In other words, each XRF signal is concurrently acquired with its corresponding beam structure, in the same flux and positioning conditions, and the imaging detector records the transmitted signal through both the sample and the mask for each GI realization. We then separate the beam structure from the sample shape computationally, during data processing. Both implementations require measuring the intensity distribution of the impinging beam on the mask. This is done either at the beginning or the end of the scan.

The required exposure times of the high-resolution imaging and XRF detectors are usually different: the imaging detector is exposed to the direct (intense) beam and therefore saturates well before the required SNR is met for the XRF signal. We circumvent this by acquiring many shorter acquisitions (e.g., exposures of 0.1 s each) for each same mask position and accumulating them. Here, we translated the large mask both vertically and horizontally, acquiring 16 and 56 positions, respectively, at a 5 mm translation step size. This amounts to 896 total GI realizations. We exposed 32 times for each GI realization for 0.1 s, amounting to 3.2 s of cumulative realization exposure time.

Data processing. GI is a computational imaging technique and requires several computational steps to recover real-space images. Our implementation requires an additional step to decouple the structure of the incoming beam from the sample transmission and to retrieve the normalization coefficients for the incoming beam-intensity variations. In this section, we describe this additional step, which is unique to our proposed setup. We refer to Section C of Supplement 1 for the full GI data processing pipeline.

If we assume that the sample transmission does not change throughout the GI acquisition, it is possible to decouple the sample transmission from the beam structure through principal component analysis (PCA). Let us represent the sample transmission with the vector $\underline{f}$ (which also includes the spatial beam-intensity profile), the beam structures for each GI realization as the set of vectors $M = \{\underline{m}_j\}$, where $j \in [1, K]$ is the index of each GI realization and K is the total number of realizations, and the beam intensity for each realization with the set of coefficients $C = \{c_j\}$. For each realization, the transmission of the sample plus the structured beam is $\underline{t}_j = c_j \underline{f} \otimes \underline{m}_j$, where $\otimes$ is the element-wise vector product. The average of all transmission images is $\frac{1}{K} \sum_j^K \{c_j \underline{f} \otimes \underline{m}_j\} = \underline{f} \otimes \frac{1}{K} \sum_i^N c_i \underline{m}_j$. The patterns in set M are supposed to be uncorrelated with each other, and $\underline{f}$ is the only component present in each transmission image $\underline{t}_j$. Thus, it is the dominant component in the PCA of the matrix $T = [\underline{t}_1, \underline{t}_2, \ldots, \underline{t}_K]$. If we split the highest PCA component from the others and reconstruct these two sets separately, we will obtain $c_j \underline{f}$ (called eigen flat field) from the former set and $\underline{m}_j$ from the latter set, for each GI realization j.
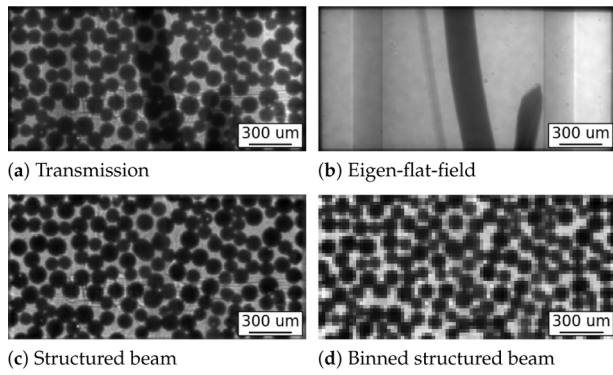
Fig. 2. (a) Transmission image of the sample with the mask. (b) Eigen flat field computed from the stack of transmission images. (c) Extracted mask from transmission (normalized and mean-subtracted). (d) Its 4×4 binned version. The intensity gradient in (a) and (b) is due to the fact that the sample is not correctly positioned at the center of the beam. This effect is correctly taken into account by the eigen-flat-field subtraction when retrieving (c).

We show an example of transmission t in Fig. 2(a), the corresponding eigen flat field in Fig. 2(b) and the beam structure in Fig. 2(c). The intensity fluctuations c_j are computed by integrating each eigen flat field $c_j f$, where $\sum_i f_i$ with $i \in [1, N]$ is the sum of all the pixels i in the image f and resulting in a constant multiplicative factor. The integrated intensities in Fig. 3(a) are in good agreement with the low-frequency trend of the corresponding Fe K_α values in Fig. 3(b). We normalize the values in Fig. 3(b) by computed intensities in Fig. 3(a), subtract the mean, and obtain the corrected GI realization intensities in Fig. 3(c).

The GI reconstruction pixel size is determined through the autocorrelation (AC) function of the structured beams [14]. Supposing that the mask is not periodic and sampled over non-overlapping regions, the resulting structured beams are not correlated with each other. Thus, it is enough to compute the AC of each structured beam with itself. The selected GI reconstruction pixel size is the lowest half-width half-maximum (HWHM) of all AC curves. More details can be found in the Supplement 1. In the presented experiment, we found a minimum HWHM equal to 4 imaging detector pixels: given its pixel size of 6 µm, it is equivalent to a 24 µm GI pixel size. Therefore, we binned the mask images 4×4, as shown in Fig. 2(d).

The GI reconstruction is performed with the primal–dual hybrid gradient (PDHG) algorithm and using the l_1-norm minimization of the isotropic Total Variation (TV) of the image [15]. The weight of the TV term is selected through cross-validation [9]. The data processing code can be found at [16].

Results. The XRF spectrum of the analyzed sample is shown in Fig. 4. The Fe and Cu peaks from the wires are clearly visible. The C K_α line of the plastic capillary is below the detection limit of the XRF detector, but lines of other elements can be seen, e.g. Zn.

In Fig. 5, we find the GI reconstructions of the Fe, Cu, and Zn XRF signals in the FoV (Fig. 5(b), Fig. 5(c), and Fig. 5(d), respectively). In Fig. 5(a), we present a color-coded composite image of the Fe, Cu, and Zn XRF signals (red, green, and blue, respectively), with superimposed edges from Fig. 2(b). This figure shows that the elemental images are in good agreement with the corresponding expected objects in the transmission image: the spatial distribution of the elements is correctly recovered (aside from artifacts). The two main types of artifacts are (a) trace signals from other channels and (b) self-attenuation. Point (a) means that the signal for one XRF line can have long tails in its energy dispersion function, and its signal can be mistakenly associated with other XRF lines. As a result, reconstructions show faint features from other elements. For instance, the Fe

Fig. 5. (a) Composite image of Fe, Cu, Zn (Red, Green, and Blue respectively), and superimposed edges of the transmission image in Fig. 2(b); and the qualitative elemental reconstructions of (b) Fe; (c) Cu; and (d) Zn. The images are affected by self-attenuation of the XRF photons. The XRF detector position is indicated with a red arrow.
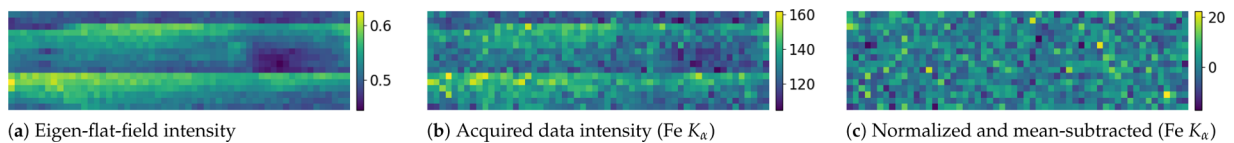

Fig. 3. (a) Integrated intensities of the eigen flat fields (Fig. 2(b)). (b) Photon counts for each GI realization of the Fe K_α line. (c) Normalized and mean-subtracted intensities for the Fe K_α line (b) by the corresponding eigen-flat-field intensities (a). Each point corresponds to one GI realization, for 16 and 56 different positions vertically and horizontally, respectively.
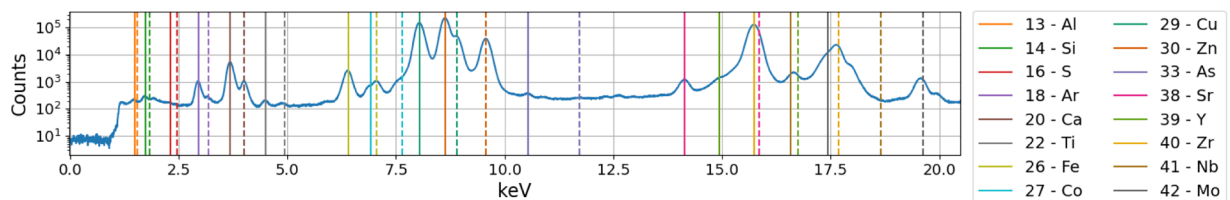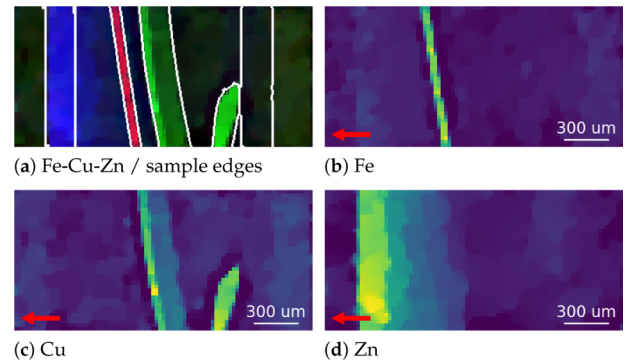

Fig. 4. XRF spectrum of the studied sample. Solid and dashed lines indicate K_α and K_β emission lines, respectively.

reconstruction (Fig. 5(b)) shows traces of the capillary on the leftmost part of the FoV. Point (b) means that the sample attenuates some of the XRF photons that it emits. As a result, regions of the sample further away from the detector have a much lower signal than regions of the sample closer to the XRF detector. This effect is clearly visible in both the Cu and Zn reconstructions (Figs. 5(c) and (d)). More specifically, the biggest Cu wire is reconstructed with a higher signal on its left side, and only the leftmost part of the capillary is reconstructed. The XRF detector is in fact positioned on the left side of the images, as seen by the transmission detector (indicated with a red arrow in Figs. 5(b)–5(d)). This type of artifact is common to all XRF methods.

The reconstructed images are approximately $1 \times 2\,mm^2$ in size, which corresponds to 42×87 pixels (for 24 µm pixel size). The acquisition consisted of 16×56 GI realizations, which represent $\sim 24.52\%$ of the reconstructed pixels.

Impact and Outlook. This proof-of-concept experiment overcomes important limitations associated with a synchrotron-based GI implementation. It demonstrates XRF-GI on a synchrotron beamline that is not otherwise suited for XRF imaging. This paves the way to enabling GI advantages (e.g., reduced dose) to synchrotron-based applications. It also enables the study of samples that could not be imaged with a PB approach because of radiation damage or the inability to move them. This includes samples that would be perturbed by the back-and-forth translation of PB acquisitions (e.g., liquids) or with heavy sample environments that could not be displaced with enough precision or speed.

In addition, the proposed XRF-GI implementation is robust against mask positioning errors or drifts, because the structure of the beam is acquired in line with the sample (without beam splitting), and simultaneously with the XRF signal. This is not the case in other GI acquisition setups. Thus, it implies a simplified setup, with fewer sources of noise or misalignment, compared to beamsplitter-based setups or computational GI approaches. Compared to PB scanning, our XRF-GI implementation is also robust against image distortions arising from drifts during an entire acquisition. The sample is visible behind the mask at each realization; thus, its position can be tracked and corrected. This could have its biggest impact at the nanoscale, where tracking drifts and positioning errors are of vital importance.

Enabling synchrotron-based XRF-GI has a direct impact on every technique that leverages the XRF signal. As an example, XAS (x ray absorption spectroscopy) often uses XRF as a high-quality proxy for the absorption signal. With XRF-GI, we enable obtaining spatial information from XAS measurements, without radically changing a beamline layout with respect to beam shaping and sample positioning. XAS measurements with PB scanning would experience dramatically increased acquisition time. An XRF-GI-based implementation would instead enable probing of large regions of the sample at once, with much fewer realizations (i.e., scanning points) than the number of pixels (by leveraging compressive sensing [9]). This would unlock routinely obtaining spatially resolved XAS maps within the time

bounds imposed by beamtime allocation. Its applications span from the study of microscopic inclusion in macroscopic naturally occurring samples to the observation of localized charge transfer phenomena in batteries.

In its current implementation, our technique requires that both the object and the mask are transparent enough to be both visible on the imaging detector at the same time. This limitation can be relaxed by scanning the mask beforehand. Even when some regions of the sample were to fully attenuate the transmitted beam, the transmission of one region of the mask in each GI realization would be enough to retrieve the correct position of the mask. This would also relax the dependency on the eigen-flat-field extraction step (i.e., using PCA), especially in the presence of sample drifts during the scan.

Disclosures.   The authors declare no conflicts of interest.

Data availability.   Data underlying the results are available at [17].

Supplemental document.   See Supplement 1 for supporting content.

REFERENCES

1. J. A. van Bokhoven, T.-L. Lee, M. Drakopoulos, C. Lamberti, S. Thieß, and J. Zegenhagen, Nat. Mater. **7**, 551 (2008).
2. F. T. Haase, A. Bergmann, T. E. Jones, J. Timoshenko, A. Herzog, H. S. Jeon, C. Rettenmaier, and B. R. Cuenya, Nat. Energy **7**, 765 (2022).
3. R. Ploeger and A. Shugar, Science **354**, 826 (2016).
4. V. Solé, E. Papillon, M. Cotte, P. Walter, and J. Susini, Spectrochim. Acta, Part B **62**, 63 (2007).
5. J. Cesar da Silva, A. Pacureanu, Y. Yang, S. Bohic, C. Morawe, R. Barrett, and P. Cloetens, Optica **4**, 492 (2017).
6. M. Vasin, Y. Ignatiev, A. Lakhtikov, A. Morovov, and V. Nazarov, Spectrochim. Acta, Part B **62**, 648 (2007).
7. J. Soltau, P. Meyer, R. Hartmann, L. Strüder, H. Soltau, and T. Salditt, Optica **10**, 127 (2023).
8. P.-A. Moreau, E. Toninelli, T. Gregory, and M. J. Padgett, Laser Photonics Rev. **12**, 1700143 (2018).
9. T. J. Lane and D. Ratner, Opt. Express **28**, 5898 (2020).
10. Y. Klein, O. Sefi, H. Schwartz, and S. Shwartz, Optica **9**, 63 (2022).
11. R. S. Bennink, S. J. Bentley, and R. W. Boyd, Phys. Rev. Lett. **89**, 113601 (2002).
12. D. Pelliccia, A. Rack, M. Scheel, V. Cantelli, and D. M. Paganin, Phys. Rev. Lett. **117**, 113902 (2016).
13. A. Gatti, E. Brambilla, M. Bache, and L. A. Lugiato, Phys. Rev. Lett. **93**, 093602 (2004).
14. A. M. Kingston, G. R. Myers, D. Pelliccia, F. Salvemini, J. J. Bevitt, U. Garbe, and D. M. Paganin, Phys. Rev. A **101**, 053844 (2020).
15. E. Y. Sidky, J. H. Jørgensen, and X. Pan, Phys. Med. Biol. **57**, 3065 (2012).
16. https://github.com/cicwi/PyCorrectedEmissionCT.
17. https://doi.org/10.5281/zenodo.7828494.